Test beam results of a high granularity LuAG fibre calorimeter prototype

2016 JINST 11 P05004

(http://iopscience.iop.org/1748-0221/11/05/P05004)

Published by IOP Publishing for Sissa Medialab

Received: *October 20, 2015*
Revised: *February 11, 2016*
Accepted: *April 15, 2016*
Published: *May 3, 2016*

2016 JINST 11 P05004

Test beam results of a high granularity LuAG fibre calorimeter prototype

A. Benaglia,[a,1] **M. Lucchini,**[a] **K. Pauwels,**[a] **C. Tully,**[b] **T. Medvedeva,**[b] **A. Heering,**[c] **C. Dujardin,**[d] **V. Kononets,**[d,e] **K. Lebbou,**[d] **N. Aubry,**[f] **S. Faraj,**[f] **G. Ferro,**[g] **P. Lecoq**[a] **and E. Auffray**[a]

[a] *European Organization for Nuclear Research, CERN, Route de Meyrin, Geneva, CH-1211 Switzerland*
[b] *Department of Physics, Princeton University, Jadwin Hall, Princeton, NJ, 08544 U.S.A.*
[c] *Department of Physics, University of Notre Dame, 225 Nieuwland Science Hall, Notre Dame, IN, 46556 U.S.A.*
[d] *Institut Lumière Matière — UMR 5306, Université Lyon 1-CNRS, Bâtiment Kastler, 10 rue Ada Byron, Villeurbanne cedex, 69622 France*
[e] *Institute for Scintillation Materials NAS of Ukraine, 60 Lenina Ave, Kharkiv, 61001 Ukraine*
[f] *Fibercryst, Parc d'Activités Wilson — Bât. A1, 31 Rue Wilson, Décines Charpieu, 69150 France*
[g] *Laboratoire des Multimatériaux et Interfaces — UMR 5615, Université Lyon 1-CNRS, Bâtiment Bertholet, 22 Avenue Gaston Berger, Villeurbanne cedex, 69622 France*

E-mail: andrea.benaglia@cern.ch

[1]Corresponding author.

doi:10.1088/1748-0221/11/05/P05004

Abstract: The progresses in the micropulling-down technique allow heavy scintillating crystals to be grown directly into a fibre geometry of variable shape, length and diameter. Examples of materials that can be grown with this technique are Lutetium Aluminum Garnets (LuAG, $Lu_3Al_5O_{12}$) and Yttrium Aluminum Garnets (YAG, $Y_3Al_5O_{12}$). Thanks to the flexibility of this approach, combined with the high density and good radiation hardness of the materials, such a technology represents a powerful tool for the development of future calorimeters. As an important proof of concept of the application of crystal fibres in future experiments, a small calorimeter prototype was built and tested on beam. A grooved brass absorber (dimensions 26 cm × 7 cm × 16 cm) was instrumented with 64 LuAG fibres, 56 of which were doped with Cerium, while the remaining 8 were undoped. Each fibre was readout individually using 8 eightfold Silicon Photomultiplier arrays, thus providing a highly granular description of the shower development inside the module as well as good tracking capabilities. The module was tested at the Fermilab Test Beam Facility using electrons and pions in the 2–16 GeV energy range. The module performance as well as fibre characterization results from this beam test are presented.

Keywords: Calorimeter methods; Calorimeters; Scintillators and scintillating fibres and light guides; Scintillators, scintillation and light emission processes (solid, gas and liquid scintillators)

2016 JINST 11 P05004

Contents

2016 JINST 11 P05004

1 Introduction

Detectors at future high energy colliders will have to withstand unprecedented operating conditions in terms of particle energy, flux and collision rates. High radiation tolerance as well as fast response will be key properties of the potential scintillator materials to be employed in such a harsh environment. Moreover, a large number of physics channels foresee multiple jets in the final state, and would therefore benefit from a hadronic jet resolution significantly better than the one of current detectors ($\sim 10\%$). For example, with 4% energy resolution for jets of 100 GeV or higher, separation of W and Z bosons via their invariant mass reconstruction in di-jet final states becomes possible.

We proposed earlier an innovative approach to meet these requirements, constituted by a total-absorption, fully active calorimeter, made of many heavy inorganic crystalline fibres grouped together in meta-crystals to form the detector blocks [1, 2]. As a matter of fact, the micropulling-down (μPD) technique allows heavy scintillating crystals to be grown directly into a fibre geometry of variable shape, length and diameter, with no need of a cutting and polishing stage as for traditional growth methods (i.e. Czochralski or Bridgman techniques). This represents a clear advantage towards a large-scale production. Lutetium Aluminum Garnet ($Lu_3Al_5O_{12}$, LuAG) was

originally considered for the assembly of the meta-crystals, thanks to its high density (6.73 g/cm^3), relatively high intrinsic light yield when doped with rare earths (e.g. approximately 25000 photons per deposited MeV with Cerium doping) and high refractive index (ranging from 2.14 at 190 nm to 1.85 at 520 nm) [3, 4]. Recent measurements confirm the good radiation tolerance of this material, showing very little radiation-induced absorption coefficients at the emission peak ($\mu_{ind} \sim 0.5\,m^{-1}$ at 520–540 nm) after γ irradiation up to an integrated dose of 100 kGy and proton irradiation up to 10^{14} cm^{-2} integrated fluence [5]. These properties make LuAG a good candidate for a scintillating calorimeter, allowing for dual-readout capabilities too, when used undoped as a Cherenkov radiator.

We reported earlier [6] about a beam test conducted at CERN in 2012, where 9 LuAG fibres of good optical quality were inserted in a small brass absorber and exposed to high energy electrons at the H2 beam line of the CERN SPS North Area. This test allowed to extract good signals from all the fibres, although a complete characterization of the physics performance of the module was limited by the small size of the prototype itself.

In this paper, a larger scale beam test, comprising 64 LuAG crystal fibres, is presented. Fibres were inserted in a grooved brass absorber and readout individually using Silicon Photomultipliers. The module was exposed to a pion and electron beam at Fermilab in March and August 2014. After a description of the experimental setup in section 2, the fibre position reconstruction is reported in section 3, and a characterization of the LuAG fibre properties is presented in section 4. Finally, the physics performance of the calorimetric module with high energy particles is presented in section 5.

2 Experimental setup

2.1 The beam line at the Fermilab Test Beam Facility

The beam we used for this test was provided by the Fermilab Test Beam Facility (FTBF). Along the MTEST beam line, the primary 120 GeV proton beam is converted into a secondary beam by a 30 cm Aluminum target, and eventually delivered to the MT6.2 experimental area by a set of quadrupole magnets and collimators. Our magnet configuration allowed secondary particles to be produced in the 1–32 GeV energy range, with a momentum resolution of $\sim 2.5\%$ or better. In this energy range, mostly electrons and pions are produced, the contamination from muons and double particle events being almost negligible. A more quantitative evaluation of the secondary beam composition can be seen in figure 1 [8].

A sketch of the experimental area hosting our setup can be seen in figure 2: a scintillation counter was located at the entrance of the hall, providing the trigger information in coincidence with the spill signals; a couple of multi-wire proportional chambers (labelled WC1 and WC2 hereafter) were situated few tens of centimeters upstream of our setup and allowed the beam position in the $x-y$ plane to be reconstructed with ~ 1 mm spatial resolution; finally, our calorimetric module was centered on the beam by means of a remotely-controlled moving table (in the x and y directions).[1]

[1]The frame of reference used throughout this paper has the x-axis horizontal on the experimental table, the y-axis pointing vertically downwards, and the z-axis aligned with the beam line and pointing in the opposite direction, as can be seen in figure 2.

2016 JINST 11 P05004

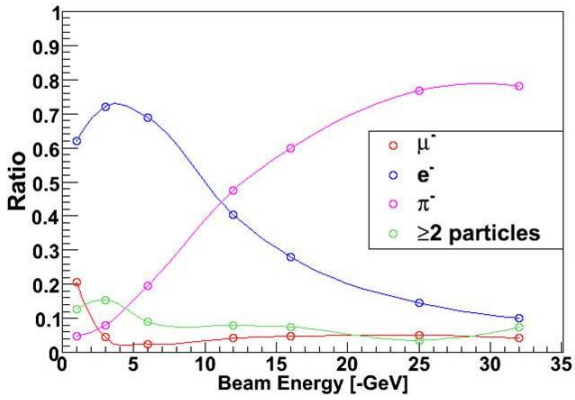

Figure 1. Secondary beam composition in the low energy pion magnet configuration (1–32 GeV) as measured by the CALICE collaboration [8].

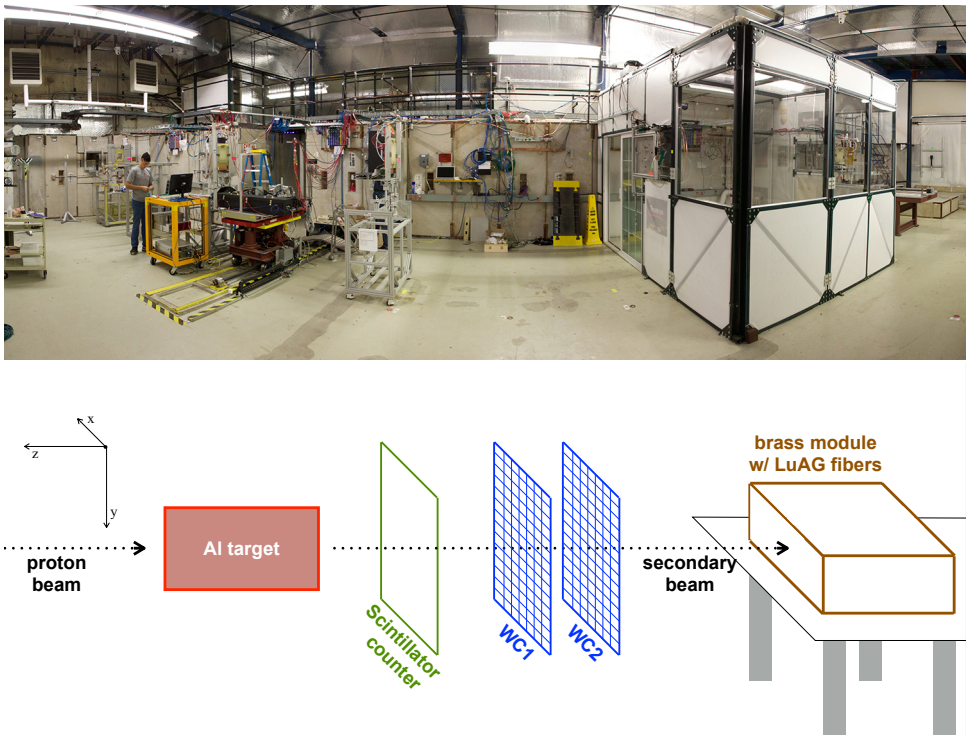

Figure 2. Picture of the experimental hall MT6.2 at the Fermilab Test Beam Facility (top). Schematic view of the secondary beam (pion and electron admixture) produced after the primary proton beam impinges onto an Aluminum target. The main components along the beam line are drawn as well (bottom).

2.2 The calorimetric module and the crystal fibres

Our calorimeter prototype (see figure 3) consisted of a grooved brass block of dimensions 255 mm × 65 mm × 160 mm. Sixty-four, 255 mm long round holes with ~ 2.6 mm diameter were drilled along the full width of the module, and arranged in 8 staggered layers of 8 holes each. The distance between the center of two adjacent holes was 4 mm, whereas 16 mm of brass separated two consecutive layers. The holes hosted 64 LuAG fibres, which were wrapped with a thin layer of Teflon at the two ends

2016 JINST 11 P05004

in order to maintain an air gap of about 0.3 mm between the fibre lateral surface and the brass absorber. The module was exposed to the beam in two different configurations, hereafter referred to as *transverse* and *pointing configurations*. In the former case, the beam was impinging at cross angle with respect to the fibres, the electromagnetic/hadronic shower developing progressively in the 8 fibre layers. In the latter, the beam was aligned with the fibres and the showers developed all along the fibre length, while laterally extending to only a few fibre layers.

When used in transverse configuration, the module size along the z axis (160 mm) corresponds to about 11 radiation lengths ($X_0 \sim 14.7$ mm) and to 0.8 pion interaction lengths ($\lambda_I \sim 200$ mm).

Round LuAG fibres were grown with the µPD technique at the *Institute of Light and Matter* (ILM, Lyon) [7] and by the company *Fibercryst*. All fibres had a diameter of 2 mm and were cut to have a length of approximately 220 mm. Of the 64 fibres we used, 55 were doped with various concentration of Cerium (LuAG:Ce) to produce scintillation light, while the remaining 9 were undoped, and therefore more suitable to detect Cherenkov light. As shown in figure 3, undoped fibres were inserted in the fourth layer of the module (layer 3), which corresponds approximately to the location of the shower maximum for 16 GeV electrons impinging onto the module in transverse configuration, and in position 63.

2.3 The photodetectors and the acquisition system

One end of each crystal fibre was coupled to a KETEK Silicon PhotoMultiplier (SiPM) using optical grease. Each SiPM had a 2.2 mm × 2.2 mm active area and was composed of 12100 cells of 20×20 µm^2 each. The breakdown voltage and the recovery time were measured in laboratory to be 25.4 V and 30 ns respectively. The choice of this particular SiPM model was mainly dictated by the photon detection efficiency (PDE), which is about 20% at the LuAG:Ce emission peak (520 nm) and is particularly high in the UV region (∼ 18% at 350 nm), which enhances the detection of Cherenkov photons produced in undoped LuAG fibres. A picture of the SiPM packages installed onto the SiPM Interface Board (SIB) and the PDE as a function of the photon wavelength can be seen in figure 4.

Two 32-channel Amplifier-Digitizer boards (PAD-E) [9], interfaced with the SIB, provided bias and signal readout from the attached SiPMs. The boards were triggered by the signal from the scintillator counter and connected to a standard PC running the acquisition software and where the data were stored. A built-in sensor allowed the temperature of the boards and the SiPMs to be continuously monitored. A temperature stabilization of $(20 \pm 1)^\circ$ C was achieved.

The PAD-E boards, originally conceived for medical physics applications, have a 20 MHz analog bandwidth and a double differentiation stage that generates a bipolar pulse. Due to the slow shaping time of the board and the ADC sampling frequency of 75 MHz (1 sample every 13.3 ns), the system was not optimized to perform timing measurements. It was nevertheless possible to clearly distinguish the fast Cherenkov signals from the slower scintillation pulses just by looking at the different pulse shape, as shown in figure 5.

In order to estimate the amount of light produced in the crystal fibres, an absolute calibration of the photodetector response was required. We used a LED driver to produce pulsed light at two different wavelengths (blue and green) that was distributed and injected into each fibre from the side opposite to the SiPM by means of clear optical fibres (see figure 6 left). During SiPM calibration runs, the trigger to the acquisition system was provided by the LED pulser itself. For most of

2016 JINST 11 P05004

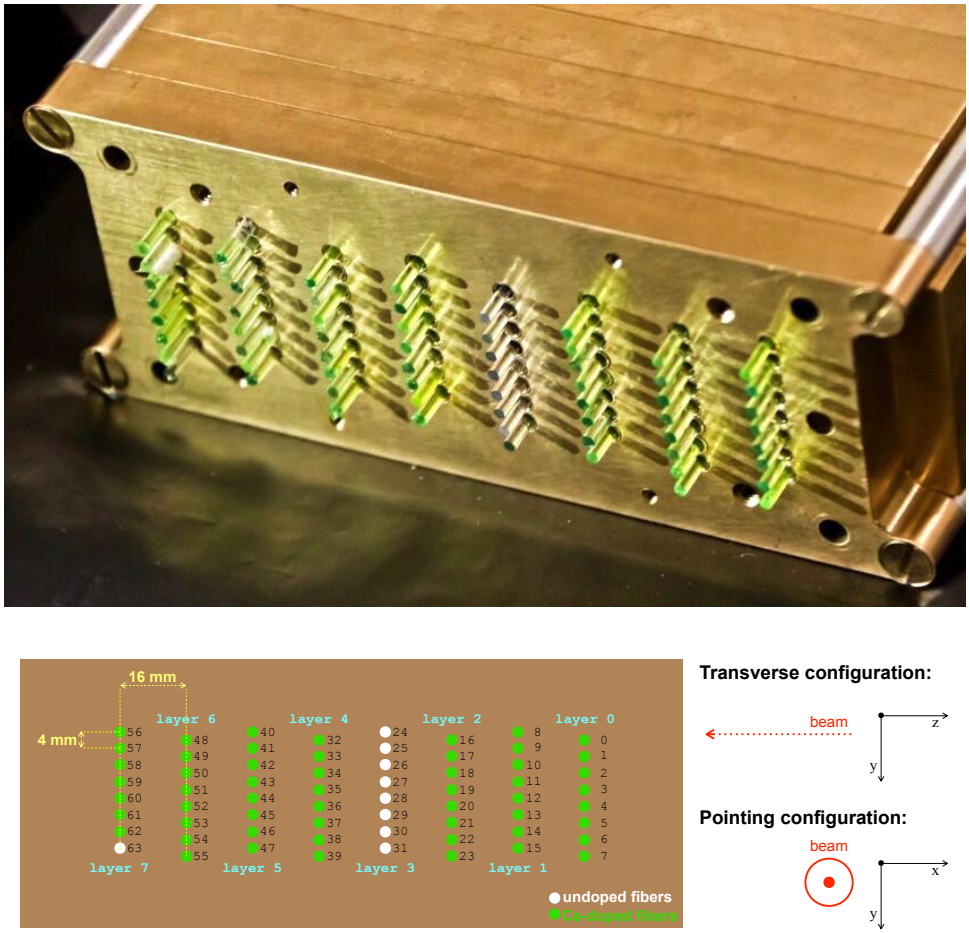

Figure 3. Picture of the grooved brass absorber loaded with crystal fibres. The fourth layer from the right contains undoped LuAG fibres, while all other layers are filled with LuAG:Ce fibres, as clearly visible from the greenish color (top). Schematic view of the module and labelling of the fibres and fibre layers. The two different beam configurations (transverse and pointing) are represented on the right, together with their respective frame of reference (bottom).

the channels, the reconstructed distribution clearly showed the signal corresponding to 0, 1, and 2 photoelectrons (ph.e.), as shown in figure 6 right, which allowed the ADC-to-ph.e. calibration factor to be extracted. Calibration constants obtained with the blue and the green LED were found to correlate, and the average of the two was taken as final value. On average, a signal of maximum amplitude of 100 ADC counts was found to correspond to about 11 ph.e. A channel-to-channel spread of about 6% in the SiPM calibration factors was observed.

2.4 Monte Carlo simulation

A detailed Monte Carlo (MC) simulation was realized by means of the GEANT4 toolkit [10, 11]. Not only the module design specifications were precisely reproduced in the MC, but also fibre properties such as the physical length and the measured light attenuation length (as will be described in section 4) were introduced in the simulation. To truthfully reproduce the beam characteristics, the

2016 JINST 11 P05004

beam in the Monte Carlo was constituted by an energy-dependent admixture of pions and electrons, following figure 1, with an angular spread of about 1 mrad in both x and y directions.

3 Module alignment and fibre position reconstruction

With the module oriented in pointing configuration, a full scan of the module surface was performed and the profile of each fibre response as a function of the beam impact point was reconstructed, thanks to the information of the wire chambers. An example of such a profile is shown in figure 7a for fibre 48. The expected profile, obtained by means of the GEANT4 simulation of the whole setup, is superimposed and in good agreement with the data.

The x and y coordinates of each fibre were reconstructed by fitting the simulated profile to the observed distribution, allowing the MC shape to translate. The results are shown in figure 7b. By fitting the expected geometrical parameters of the module to the reconstructed fibre positions, a distance of (16.1 ± 0.1) mm between fibre layers along x and (3.7 ± 0.1) mm between adjacent fibres along y is found, in good agreement with the module specifications. This measurement allowed the module to be correctly centered on the beam.

4 Fibre characterization

This section is devoted to the characterization of the fibre performance. The response of individual fibres to high energy electrons and pions was studied with the calorimetric module in both transverse and pointing configuration, thus allowing for a measurement of the fibre attenuation length and light output.

4.1 Fibre attenuation lengths

A non-uniformity along the fibre length in the efficiency of the light extraction at the fibre ends can seriously affect the performance with high energy showers, especially if the excitation volume

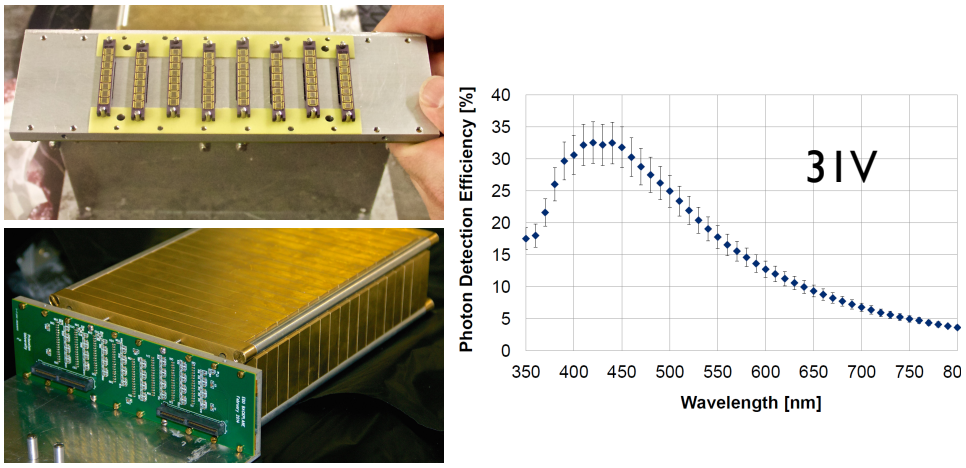

Figure 4. The 8 eightfold KETEK SiPM packages used to read out each crystal fibre individually, mounted on the SiPM Interface Board (left). The SiPM PDE as measured in laboratory (right).

2016 JINST 11 P05004

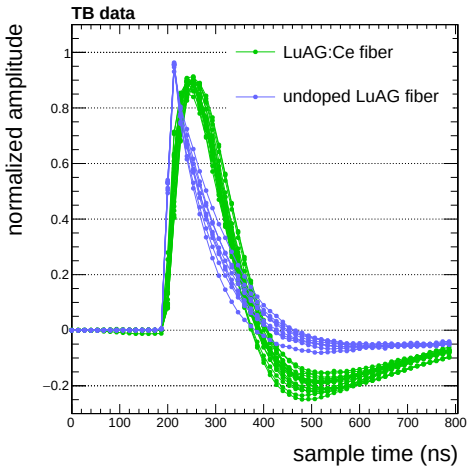

Figure 5. Normalized pulse shape for various Cerium-doped fibres (green) and undoped LuAG fibres (blue). In undoped fibres, the promptly emitted Cherenkov photons give rise to a faster pulse than scintillation photons, which instead dominate the signal in doped fibres.

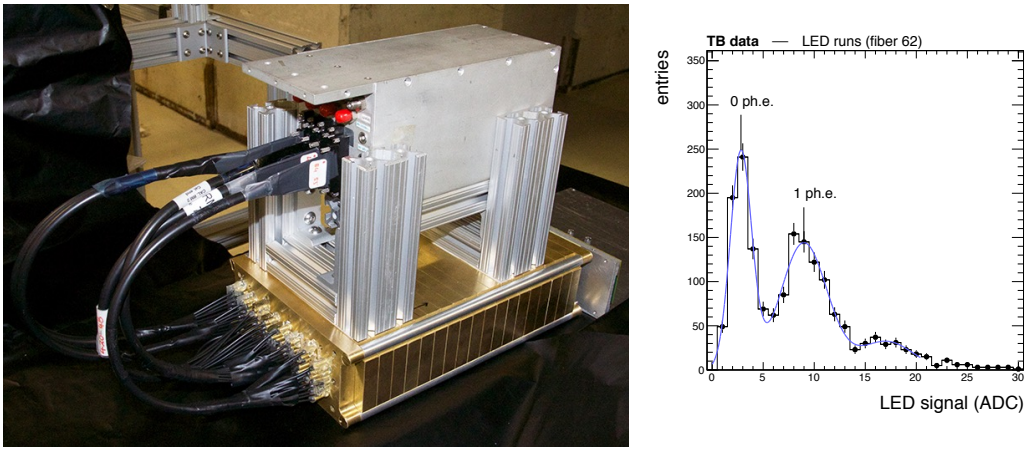

Figure 6. LED pulser and clear fibre distribution system to inject LED light into the fibres (left). SiPM signal of fibre 62 when LED blue light was injected at the opposite end. The peaks corresponding to 0 and 1 ph.e. detected are clearly visible, whereas the 2 ph.e. peak is not fully resolved (right).

expands over a large portion of the fibre (e.g. if the fibre axis is at small angle with the beam line). This is why a measurement of the amount of extracted light as a function of the excitation distance from the SiPM is fundamental. For most of the fibres, a characterization of the attenuation length was initially performed in laboratory at CERN. In a dedicated bench, both a radioactive ^{22}Na source and a LED pulser were used to excite the fibres at variable distance from the photodetector [12].

The measurement was repeated at the FTBF with high energy particles. The calorimetric module was exposed to a 16 GeV electron+pion beam in transverse configuration, positioning the table at various (x, y) coordinates to obtain a nearly uniform scan of the entire length of the fibres. To enhance the signal, only events in which the beam was impinging within ±2 mm from the fibre center along the y axis were selected for the computation of the energy deposit of each fibre. The

2016 JINST 11 P05004

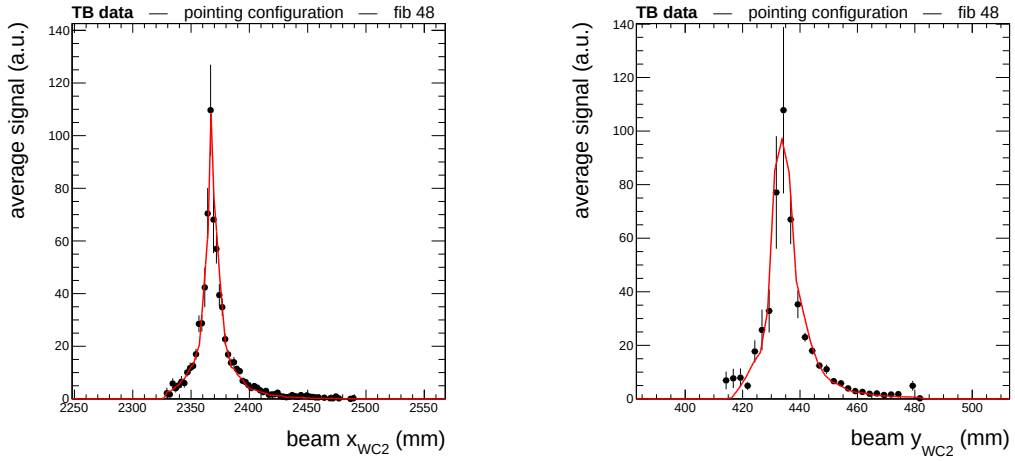

(a)

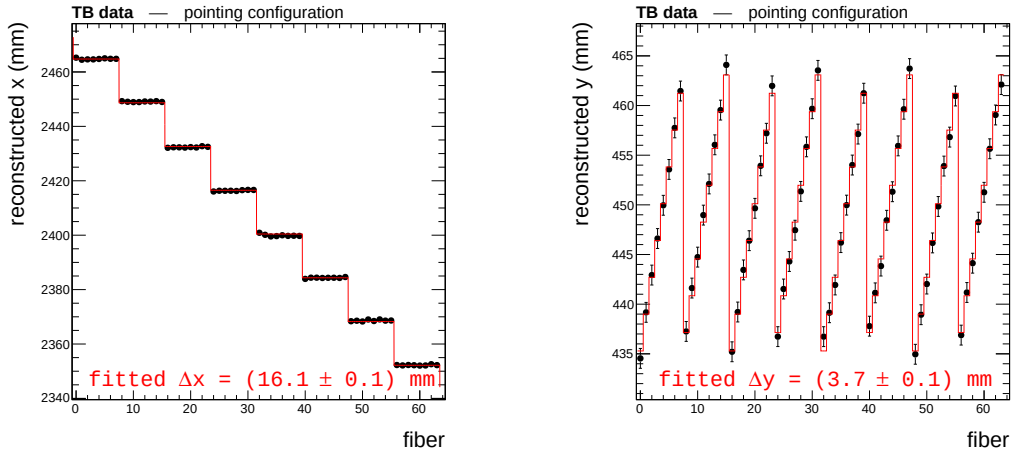

(b)

Figure 7. (a) Average response profile of fibre 48 as a function of the beam impact x (left) and y (right) coordinate, as reconstructed by WC2 (solid black points). The simulated profile is superimposed (red line). (b) Reconstructed x (left) and y (right) coordinates of all fibre centers from a fit to the energy profiles as in top figures.

transverse light output (LO) profiles of each fibre were then analyzed, parametrizing the LO as

$$\mathrm{LO}(x) = \mathrm{LO}_0 \cdot e^{-x/\lambda_{\mathrm{att}}} + c\,, \tag{4.1}$$

where x is the beam distance from the SiPM, LO_0 is the light output in proximity to the SiPM, λ_{att} is a parameter expressing the characteristic light attenuation length in the fibre and c is a constant value. An example of such profiles and the corresponding fit is shown in the left plot of figure 8, whereas on the right plot the fitted λ_{att} for all the 64 fibres is shown as a function of the fibre light output. The LO is here expressed as the number of ph.e. detected per deposited MeV (for the evaluation of the expected energy deposition in the fibres, see the next paragraph). As can be seen, the fibre quality largely varies, with attenuation lengths of few centimeters only to almost 40 cm for the best samples. This variation mostly depends on the fibre growth parameters, such

2016 JINST 11 P05004

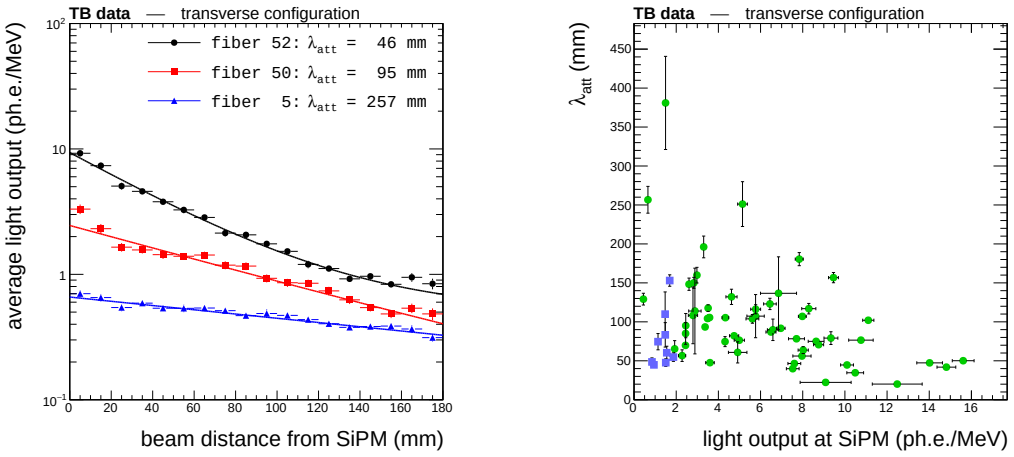

Figure 8. Attenuation profiles for three different fibres (fibre 5, 50, and 57) and the corresponding fit function, using equation (4.1). Different values of λ_{att} are found (left). Attenuation length of all the 64 fibres plotted versus the fibre light output (LO). The LO is obtained from the fit function extrapolation at 0 distance from the SiPM, so that the effect of light attenuation is negligible. Green dots and blue squares represent LuAG:Ce and undoped LuAG fibres, respectively (right).

as pulling speed, crucible temperature, and Cerium concentration. In particular, figure 8 right shows that attenuation lengths in excess of ~ 200 mm are only measured in fibres with relatively low light output, whereas the brightest fibres in our sample (LO larger than ~10 ph.e./ MeV) had poor attenuation lengths (50 mm or less). This can be explained with larger Ce concentration being responsible for both higher light output and higher probability of light self absorption [13, 14] as well as Ce-related defects arising during the growth process.

The attenuation profiles measured at the beam test were found to well agree with laboratory measurements, as shown in figure 9. This was an important step to cross-check and validate the fibre characterization procedure in laboratory.

4.2 Light output measurement

The fibres used in this beam test were grown with different Cerium concentrations, ranging from ~ 0 for undoped fibres to up to ~ 600 ppm for highly doped ones. Moreover, fibres differed in the quality of the optical surface and in the presence of internal defects, both affecting the light transmission. Therefore, large fibre-to-fibre differences in the amount of both produced and extracted light were expected.

The average signal measured at the SiPM with the module in both the transverse and the pointing configuration can be used to measure the light output of the fibres, that is the light extracted from a fibre end per deposited MeV. Light propagation effects need to be properly accounted for in the measurement, in order that the LO be disentangled from them.

In transverse configuration, the extrapolation at 0 distance from the SiPM of the signal attenuation profiles represents an estimate of the light extracted in case of a perfectly transparent fibre (i.e. no light loss due to absorption or diffusion effects). To turn this number into LO, the knowledge of the average energy (in MeV) deposited by electron and pions in the fibres is required. This was estimated using the GEANT4 simulation, as shown in figure 10 left. In particular, given the

2016 JINST 11 P05004

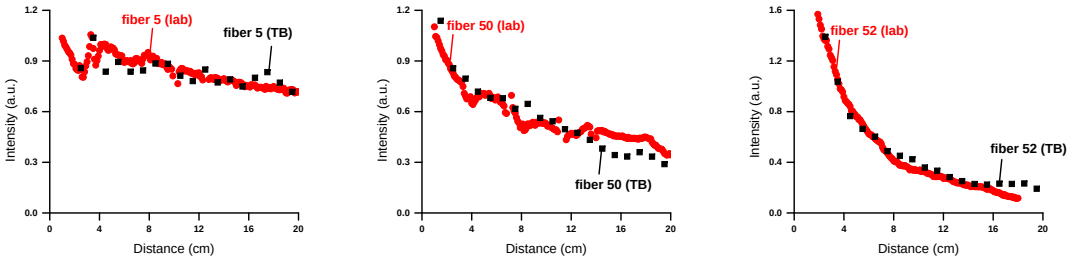

(a)

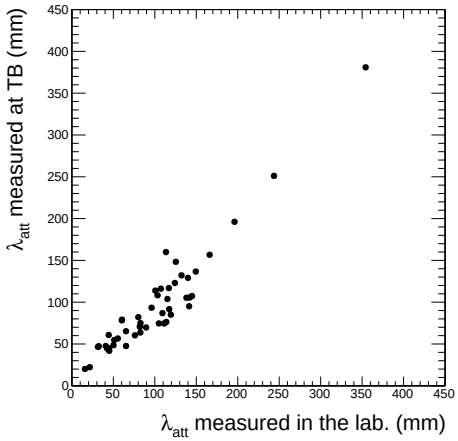

(b)

Figure 9. (a) Attenuation profiles for three different fibres (fibre 8, 14, and 52) as obtained in laboratory (red points) and at the beam test (black squares). (b) Scatter plot showing the attenuation length as measured at the beam test vs. the same parameter extracted from laboratory measurements.

electromagnetic shower development in the module in transverse configuration, the average energy deposit is not flat with respect to the fibre depth in the brass, but exhibits a maximum around the 4^{th} or 5^{th} fibre layer. The measured LO is shown in figure 11 left. On average, Ce-doped fibres yielded about 6 ph.e. per deposited MeV, while the LO from Cherenkov light in undoped fibres was about 1.5 ph.e. per deposited MeV. A few fibres yielded a very small amount of light, which can be attributed to a bad coupling to the SiPM, while few others yielded up to about 15 ph.e. per MeV due to a higher Cerium concentration.

With the module oriented in pointing configuration, the estimate of the fibre LO was more complicated. First of all, since the showers developed all along the fibre length, it was more difficult to disentangle the effect of light attenuation from the measured light output. The simulation was used to estimate the amount of light actually reaching the SiPM by attenuating, channel by channel, the light generated along the fibre according to the measured attenuation profiles (in figure 10 right, the energy deposition profile as a function of the beam transverse distance from the fibre axis is shown for a perfectly transparent fibre, i.e. in which the LO is not affected by attenuation effects). An additional source of complexity came from the saturation of the ADC channels, occurring especially in bright fibres and when the beam was impinging at small distance from the fibre axis. The estimate of the LO was obtained from a fit of the tails of the measured energy profiles,

2016 JINST 11 P05004

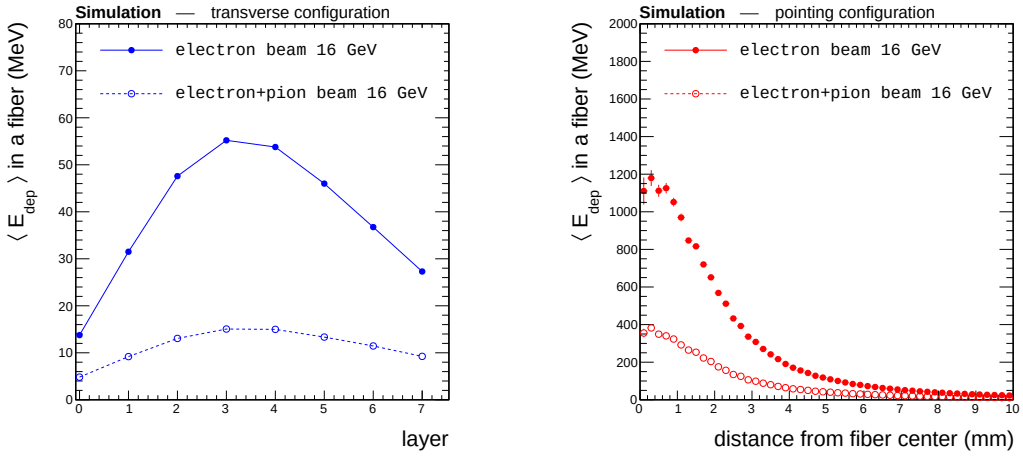

Figure 10. Average energy deposited in a single fibre as a function of the fibre layer in the absorber module, as predicted by the simulation. Fibres are at cross angle with respect to the beam. Only events in which the beam distance from the fibre center was such that $|\Delta x| < 80\,\text{mm}$ and $|\Delta y| =< 2\,\text{mm}$ were selected. A pure electron beam as well as an admixture of electrons and pions are simulated, as expected from the beam specifications of the FTBF MT6 line, as in figure 1 (left). Profile of energy deposition in a perfectly transparent fibre (i.e. no effects of attenuation length) as a function of the distance of the incoming particle from the fibre axis, when fibres are parallel to the beam direction (right).

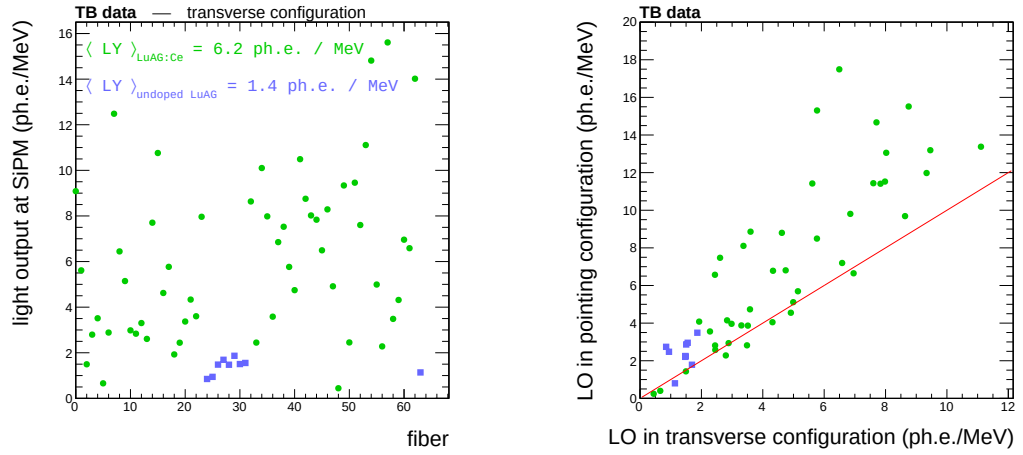

Figure 11. Estimated light output, expressed in ph.e. per deposited MeV, for all the 64 fibres with the module in transverse configuration (left). Correlation between the measured LO in transverse and pointing configuration (right). Green dots and blue squares represent LuAG:Ce and undoped LuAG fibres respectively.

where the fraction of saturated events was negligible, using the simulated profiles as fit templates. Despite a lesser accuracy, a correlation of the LO obtained in pointing configuration with the one estimated in transverse configuration was observed, as shown in figure 11 right. For undoped fibres, a systematically larger LO is observed, with the ratio $\text{LO}_{\text{pointing}}/\text{LO}_{\text{transverse}}$ being ~ 1.7. This can be attributed to the non isotropic emission of Cherenkov light, which favors its extraction in pointing configuration.

2016 JINST 11 P05004

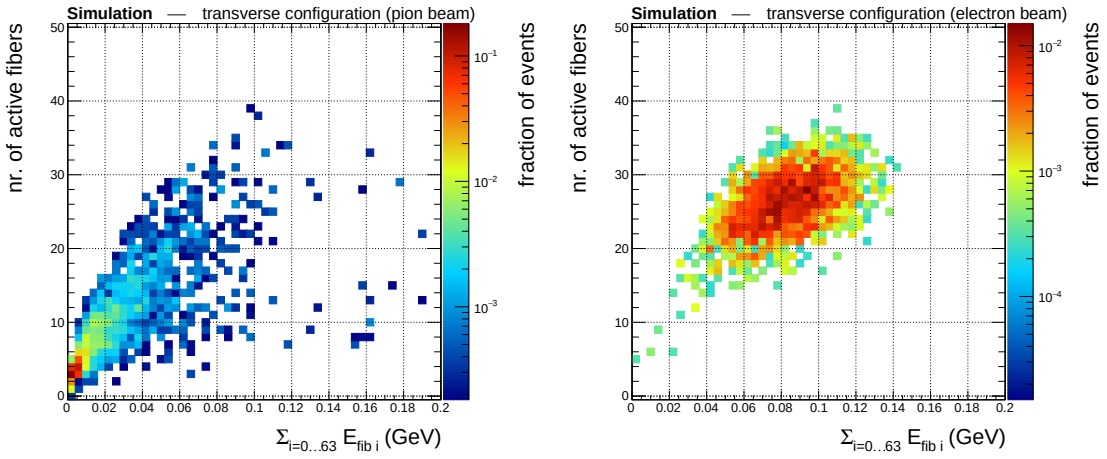

Figure 12. Simulation plot representing the number of active fibres (i.e. the number of fibres with a deposited energy above a given threshold) vs. the sum of the energy deposits in all the fibres, for pions (left) and electrons (right). The different signature of the two particle species in the calorimetric module is visible. An incident beam energy of 8 GeV is assumed, and only particles impinging in a region of $\Delta x = \pm 10$ mm and $\Delta y = \pm 7.5$ mm around the center of the module are considered.

5 Performance of the calorimetric module

In this section, the measured performance of the crystal fibre module with high energy particles is reported. In particular, the potential for particle identification and the energy resolution are discussed.

5.1 Particle identification

The high granularity of our calorimetric module was exploited to identify the nature of the impinging particle (electrons vs. pions), based on the multiplicity of active fibres. Due to the small size of our module compared to the characteristic interaction length of pions in brass (160 mm vs. $\lambda_I \sim 200$ mm), pions behaved like minimum ionizing particles, depositing a small amount of energy in only few (≤ 8) fibres, whereas in the case of electrons, the electromagnetic shower was almost fully contained in the module, with a larger fraction of energy deposited in a higher number of fibres (≥ 20). The different behavior of electrons and pions is illustrated in figure 12, where a scatter plot of the number of active fibres versus the total energy deposited in the fibres is shown for the two particle species, as derived by the simulation.

When analyzing the beam test data, a fibre was considered to be active if the signal was larger than 10 times the standard pedestal fluctuation, which corresponded to 15 ADC counts. By requiring that the number of active fibres per event was larger than $13 + 4 \cdot \log_2 E_{\text{beam}}$, an effective rejection of pion events was achieved, and the expected electron purity of figure 1 was reproduced, as shown in figure 13.

5.2 Energy resolution and linearity

Beam energies ranging from 2 to 16 GeV were used to study the response of the calorimetric module to high energy electromagnetic showers. In this energy range, the showers were reasonably

2016 JINST 11 P05004

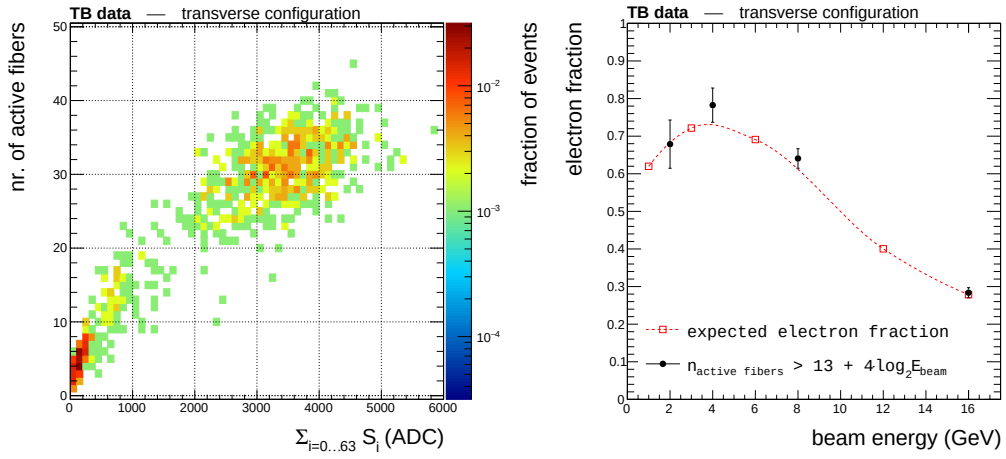

(a) **(b)**

Figure 13. (a) Scatter plot of the number of active fibres vs. the sum of the signal amplitudes in all the fibres, as seen in beam test data for 8 GeV impinging beam. (b) Fraction of events surviving after the cut on the number of active fibres, compared to the expected electron fraction as measured by the CALICE collaboration, cf. figure 1.

contained in the module, the maximum being located around the 3$^{\text{rd}}$ or 4$^{\text{th}}$ fibre layer, and a satisfactory electron purity (between 30 and 80%) was provided by the beam line. Higher beam energies were not taken into account due to a too low electron purity ($\leq$ 10%) and to an increasingly larger shower leakage outside the module. The pion background was rejected applying the cut on the number of active fibres described in the previous paragraph. To allow for the electromagnetic showers to be well sampled by the fibres, only events where the beam was impinging in a region of transverse dimensions 20 mm $\times$ 15 mm around the centre of the module were considered in the analysis.

Figure 14a shows the distributions of the response of the whole module for different beam energies, obtained by summing the signal of all the fibres. In order to account for the large variations in the fibre-to-fibre response, as described in section 4.2, an intercalibration factor was computed and applied to each individual signal. Fibres belonging to the same fibre layer were equalized by extrapolating, for each of them, the measured LO profile (eq. (4.1)) to the point corresponding to the centre of the module ($\hat{x}$ = 110 mm). The inverse of this value, normalized by the average LO in that fibre layer, was taken as the fibre intercalibration coefficient, under the assumption that fibres at the same depth in the brass absorber should provide the same average response upon an uniform transverse beam profile. The different fibre layers were then intercalibrated by adjusting the average layer response in data according to the longitudinal shower profile predicted by the simulation using 8 GeV electron events. Summarizing, the whole module amplitude can be written as

$$S_{\text{tot}} = \sum_{i=0}^{63} c_i \cdot S_i \,, \tag{5.1}$$

where S_i is the signal amplitude measured in fibre i in ADC and $c_i = \eta_{\text{layer}} \cdot \left[\text{LO}_i(\hat{x})/\langle \text{LO}_i(\hat{x})\rangle_{i\in\text{layer}}\right]^{-1}$ is the calibration coefficient, η_{layer} being the layer-to-layer scale calibration factor. The response

2016 JINST 11 P05004

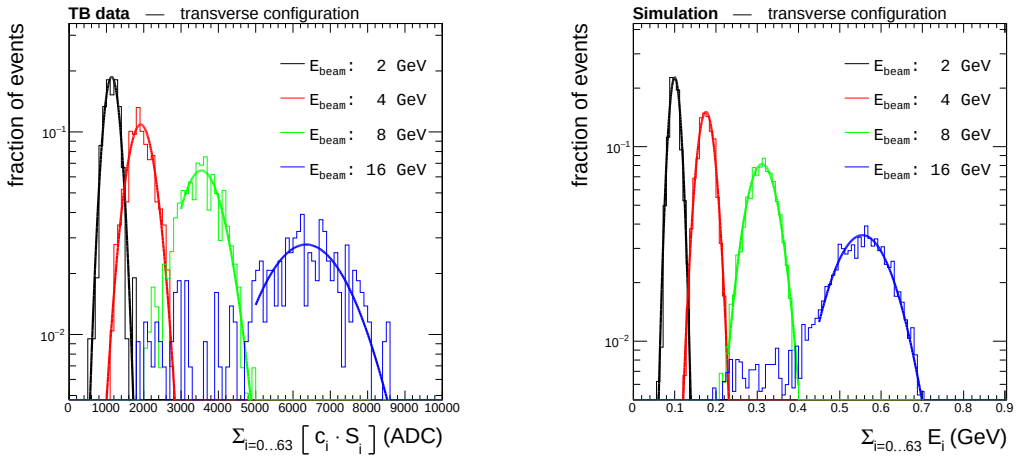

(a)

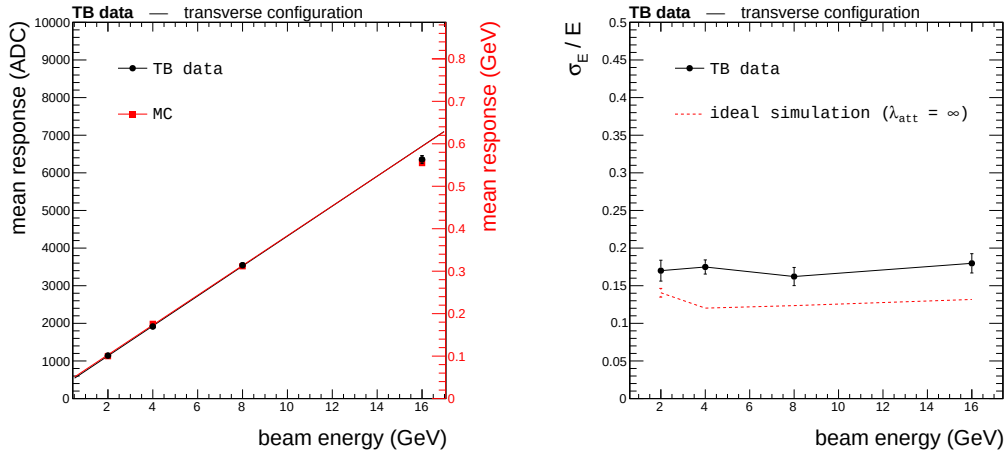

(b) **(c)**

Figure 14. (a) Distribution of signal amplitudes obtained by the sum of the intercalibrated signals from all the fibres, for different beam energies. Beam test data are shown on the left, whereas the expected MC distribution are shown on the right. (b) Linearity of the response for TB data (black dots) and MC simulation (red squares). For each beam energy point, the mean response is obtained from a Gaussian fit to the signal amplitude distributions shown in (a). A linear function is fitted to data and MC points for beam energies between 2 and 8 GeV. The resulting function is superimposed (black and red line, respectively). Deviation from linearity at 16 GeV is due to increased shower leakage. Data and simulation points in the figure correspond to the left and right y-axis, respectively. (c) Energy resolution of the calorimetric module as measured in the data (black dots) compared to expectations from an ideal simulation, i.e. fibres have an infinite attenuation length.

of the calorimetric module was measured to be linear to within 0.7% up to 8 GeV, with a $\sim$ 5% deviation from linearity at 16 GeV due to an increased longitudinal shower leakage. This effect is confirmed by the simulation, as shown in figure 14b.

From a Gaussian fit to the signal amplitude peaks, the energy resolution of the calorimetric module was estimated. The performance was limited by the small module size and the consequent longitudinal shower leakage. The result, shown in figure 14c, is compared with the expectation from an ideal MC simulation where light propagation effects can be neglected, representing the

2016 JINST 11 P05004

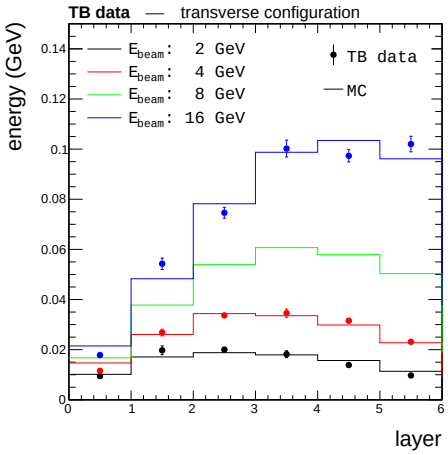

Figure 15. Profile of the longitudinal development of electron shower in the module for different beam energies. Colored dots represent the average signal in each fibre layer as measured in the data, whereas lines show the expected profile as predicted by the simulation. Data points are not shown for 8 GeV beam energy since they were used to derive layer-to-layer intercalibration factors.

ultimate performance limit of our experimental setup. The energy resolution observed in the data has roughly and additional 12% contribution added in quadrature to the MC limit, which is most likely due to the finite λ_{att} of the fibres and the limited precision of the intercalibration procedure.

5.3 Longitudinal energy profile

The high granularity of our calorimetric prototype provided useful information to study the shower shape on an event-by-event basis. Selecting electron events with the same criteria used to study the energy resolution discussed in the previous paragraph, the longitudinal shower profile was reconstructed by adding the signal from the fibres belonging to the same vertical layer and displaying the average amplitude as a function of the fibre layer. Figure 15 shows the shower profile as measured in data and compared to the expectation from the MC simulation. A good level of agreement is found. Unfortunately, due to a malfunction of the voltage supplier, the SiPMs of the last two layers were not operational during these runs, which limited the measurement to the first six fibre layers.

6 Conclusions

This beam test confirmed the potential of crystal fibres for calorimetry applications. The crystal fibre prototype tested at the Fermilab Test Beam Facility confirmed the importance of high granularity for an effective separation of electron from pion events. The module response linearity and the electron shower longitudinal profiles were studied with high energy particles and found to well agree with simulation predictions.

The most important factors still limiting the performance of the module for calorimetric measurements were found to be non-uniformities in the light yield and light collection efficiency of the fibres. The large number of channels in this prototype implied the selection of fibres belonging to different production batches, in which different growth parameters and conditions were used. The characterization of the fibre response obtained with this beam test will help identify a set of

2016 JINST 11 P05004

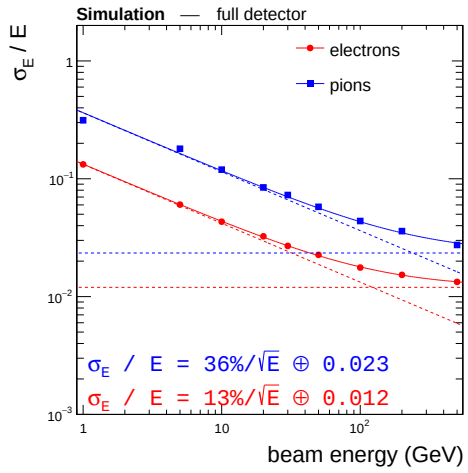

Figure 16. Intrinsic energy resolution of a brass+ LuAG fibre calorimeter. Fibre arrangement is the same as the one of the small prototype tested on beam.

optimized parameters for the growth of fibres with good properties for calorimetry applications. A good reproducibility of the fibre optical quality is a crucial point towards a large-scale fibre production for a high granularity detector.

In addition to that, the still limited module dimension prevented a full sampling of the particle shower, especially at high energy. In order to evaluate the intrinsic potential of a crystal fibre calorimeter, a full-size detector was simulated with GEANT4 using the same materials and fibre arrangement as in our prototype, and assuming good attenuation lengths for all the fibres (> 20 cm). As shown in figure 16, such a configuration would ensure a good reconstruction performance of both electrons and pions, with a small constant term ($\lesssim 2\%$) contributing to the energy resolution at high energy.

Acknowledgments

Research is conducted in the frame of the Crystal Clear Collaboration. We acknowledge support from the French National Agency for Research under grand agreement ANR-10-BLAN-0947 (INFINHI). This research project is supported by a Marie Curie Early Initial Training Network Fellowship of the European Union's Seventh Framework Programme (FP/2007-2013) under Grant Agreement Agreement 289355-PicoSEC-MCNet. The funding support for the Princeton University group comes from DOE Award n°ER-41850. We would like to thank all Fermilab experts and technicians of the FTBF division for making the test beam facility available, and in particular Paul Rubinov for providing the PAD-E boards for readout and constant support.

References

[1] P. Lecoq, *Metamaterials for novel X- or γ-ray detector designs*, in proceedings of the *2008 IEEE Nuclear Science Symposium, Medical Imaging Conference and 16th Room Temperature Semiconductor Detector Workshop*, Dresden, Germany, October 19–25 2008, pp. 680–684.

[2] P. Lecoq, *New crystal technologies for novel calorimeter concepts*, *J. Phys. Conf. Ser.* **160** (2009) 012016.

2016 JINST 11 P05004

[3] Y. Kuwano, K. Suda, N. Ishizawa and T. Yamada, *Crystal growth and properties of* $(Lu,Y)_3Al_5O_{12}$, *J. Cryst. Growth* **260** (2004) 159.

[4] C. Dujardin et al., *LuAG:Ce fibers for high energy calorimetry*, *J. Appl. Phys.* **108** (2010) 013510.

[5] M.T. Lucchini, K. Pauwels, K. Blazek, S. Ochesanu and E. Auffray, *Radiation Tolerance of LuAG:Ce and YAG:Ce Crystals under High Levels of Gamma- and Proton-Irradiation*, *IEEE Trans. Nucl. Sci.* **63** (2016) 586.

[6] M.T. Lucchini et al., *Test beam results with LuAG fibers for next-generation calorimeters*, 2013 *JINST* **8** P10017.

[7] X. Xu et al., *Ce-doped LuAG single-crystal fibers grown from the melt for high-energy physics*, *Acta Mater.* **67** (2014) 232.

[8] http://ppd.fnal.gov/ftbf/beam/CaliceChart.jpg.

[9] P. Rubinov et al., *T-1043: Measurements of Photoelectron Yields for Prototype Mu2e Cosmic Ray Veto Scintillation Counters*, FERMILAB-PROPOSAL-1043 (2013).

[10] GEANT4 collaboration, S. Agostinelli et al., *GEANT4: A Simulation toolkit*, *Nucl. Instrum. Meth.* **A 506** (2003) 250.

[11] J. Allison et al., *Geant4 developments and applications*, *IEEE Trans. Nucl. Sci.* **53** (2006) 270.

[12] K. Pauwels et al., *Single crystalline LuAG fibers for homogeneous dual-readout calorimeters*, 2013 *JINST* **8** P09019.

[13] F. Auzel et al., *Radiation trapping and self-quenching analysis in* Yb^{3+}, Er^{3+}, *and* Ho^{3+} *doped* Y_2O_3, *Opt. Mater.* **24** (2003) 103.

[14] D. Weele, D. Schaart and P. Dorenbos, *The Effect of Self-Absorption on the Scintillation Properties of* Ce^{3+} *Activated* $LaBr_3$ *and* $CeBr_3$, *IEEE Trans. Nucl. Sci.* **61** (2014) 683.

2016 JINST 11 P05004